Systematic analysis of the neutron-induced reaction cross sections for ^{nat}Mo isotopes within 10–20 MeV

Siddharth Parashari,[1,*] S. Mukherjee,[1,†] S. V. Suryanarayana,[2] B. K. Nayak,[2] Rajnikant Makwana,[1] N. L. Singh,[1] and H. Naik[3]

[1]*Department of Physics, Faculty of Science, The Maharaja Sayajirao University of Baroda, Vadodara 390002, India*
[2]*Nuclear Physics Division, Bhabha Atomic Research Center, Mumbai 400085, India*
[3]*Radiochemistry Division, Bhabha Atomic Research Center, Mumbai 400085, India*

The production cross sections for the medical isotope ^{99}Mo were measured using the ^{100}Mo$(n, 2n)$ reaction at average neutron energies of 10.95 ± 0.45, 13.97 ± 0.68, 16.99 ± 0.53, and 20.00 ± 0.58 MeV using offline γ-ray spectroscopy. The neutron beam was generated using the ^{nat}Li(p, n) reaction at the 14UD BARC-TIFR Pelletron facility, Mumbai, India. The uncertainties in the measured data were calculated using covariance analysis. The experimental results were compared with the existing data libraries ENDF/B-VII.1, JENDL-4.0, JEFF-3.2, and CENDL-3.1. The present results were also reproduced and compared with the theoretical nuclear model codes TALYS-1.9 and ALICE-2017 using different input descriptions. A modified set of parameters were also used in TALYS-1.9 to fit the existing data more accurately. The present findings show a good agreement with the theoretical predictions and with the existing experimental results from the different data libraries. In addition to this, a comparative study have also been performed between the literature data of (n, p), $(n, 2n)$, and (n, α) reaction cross sections at 14.5 MeV using various systematic formulas. The outcomes of the present work are important for the advancement of medical accelerators, dosimetry, and fast reactor systems.

I. INTRODUCTION

Molybdenum is among the five refractory metals because of its ability to handle intense heat and pressure. Its resistance to high temperatures, corrosion, and pressure makes it a strong candidate to be used in nuclear reactors such as accelerator-driven subcritical systems (ADSs) [1,2] and the International Thermonuclear Experimental Reactor (ITER) [3]. Molybdenum naturally occurs with seven isotopes, ^{92}Mo (14.8%), ^{94}Mo (9.2%), ^{95}Mo (15.9%), ^{96}Mo (16.7%), ^{97}Mo (9.6%), ^{98}Mo (24.1%), and ^{100}Mo (9.6%). The isotopes of molybdenum have several other applications, such as hard steel alloy production, uses in the petroleum industry, as a trace element for plants and animals, and most importantly to produce ^{99m}Tc, which is widely used in medicine for imaging and diagnostics. It decays by readily detectable γ rays of energy 140.5 keV [4]. At present ^{99m}Tc is used for about 80% of imaging procedures [5,6], such as single photon emission computed tomography (SPECT), bone and brain scans, myocardial perfusion imaging (MPI), and many more.

There are various reaction channels which can be used for the production of the ^{99m}Tc isotope. The ^{99m}Tc isotope can be produced instantly by using ^{100}Mo$(p, 2n)$ [7–10] and ^{238}U(p, f) [10] channels. However, the reactions demand a high flux of protons due to the short half-life of the product. One of the conventional channels of producing ^{99}Mo is by

using ^{235}U(n, f) and ^{98}Mo(n, γ) reactions in nuclear reactors. The ^{235}U isotope in the form of high enriched uranium (HEU, 93%) and low enriched uranium (LEU, 20%) is used for the production of the isotope ^{99}Mo. The cost, safety, waste management, and licensing makes the production of ^{99}Mo from either HEU or LEU unfavorable. The ^{238}U(γ, f) and ^{100}Mo(γ, n) reactions can be an alternative to the above reaction channels [5,11] within 30 MeV photon energies. Sufficient data are also available in EXFOR [12] for ^{100}Mo(γ, n) reaction at different photon energies. In addition to the above, the ^{96}Zr(α, n) reaction can also serve as a route to produce the ^{99}Mo isotope.

Among all the possible reaction channels to produce ^{99m}Tc, the reaction ^{100}Mo$(n, 2n)^{99}$Mo may be the most suitable. Experimentally measured data from different authors [13–21] based on the D+D or D+T reactions (where D and T denote ^{2}H and ^{3}H, respectively) and by using the ^{7}Li(p, n) reaction [22] are available in the EXFOR database [12] from threshold to 20 MeV neutron energies. However, most of the measured data are concentrated around 14 MeV. In the present work, we have measured ^{100}Mo$(n, 2n)^{99}$Mo reaction cross sections for 10.95 ± 0.45, 13.97 ± 0.68, 16.99 ± 0.53, and 20.00 ± 0.58 MeV neutron energies using the ^{nat}Li(p, n) reaction as neutron generator. The flux was measured using the ^{27}Al$(n, \alpha)^{24}$Na reaction. The uncertainties in the measured data were calculated using the error propagation method [23]. The measured data were compared with theoretical data libraries ENDF-B/VII.1 [24], JENDL-4.0 [25], JEFF-3.2 [26], and CENDL-3.1 [27]. The data were also reproduced and compared with the theoretical model codes TALYS-1.9 [28] and ALICE-2017 [29], using

*siddharthparashri5@gmail.com
†sk.mukherjee-phy@msubaroda.ac.in

default as well as modified input parameters for the selection of the nuclear models and nuclear level densities. Since Mo is considered for use in the modern reactor technology [21] as an alloying material, the hydrogen and helium production cross sections are of particular interest. In the present investigations, the systematic formulas proposed by different authors [30–40], over the years, were used in order to provide a better insight into the analysis. These systematic formulas were used for the calculation of the (n, p), $(n, 2n)$, and (n, α) reaction cross sections as well as to compare the measured data with the calculated results. The present work incorporates the experimental cross section data for the $^{100}\text{Mo}(n, 2n)^{99}\text{Mo}$ reaction at the four neutron energies within a proper theoretical framework along with the systematic study of different possible neutron-induced reaction channels of Mo isotopes using theoretical formulas. The preliminary results from the present work have also been presented elsewhere [41].

II. EXPERIMENTAL METHODOLOGY

The experiment was carried out by using the 14UD Bhabha Atomic Research Center–Tata Institute of Fundamental Research (BARC-TIFR) Pelletron facility in Mumbai, India, using the activation technique followed by offline γ-ray spectroscopy. The neutron beams of desired energies were generated using the $^{\text{nat}}\text{Li}(p, n)$ reaction. A lithium (Li) target of thickness ≈ 6.8 mg/cm^2 was used in between two tantalum (Ta) foils of different thicknesses. A Ta foil of thickness ≈ 4 mg/cm^2 was used at the front of the Li foil and the other Ta foil of thickness 0.1 mm was used at the back of the Li to prevent protons from striking the target. Behind the Ta-Li-Ta stack, molybdenum (Mo) metal foils of thickness 0.1 mm were placed at a distance of 2.1 cm, aligned at zero degrees with respect to the proton beam for each irradiation. An aluminum metal (monitor) foil of thickness 0.1 mm was placed together with each Mo (sample) to evaluate the neutron flux. The areas of both the monitor and the sample foils were taken as 1×1 cm^2 in order to avoid area corrections in the flux. A schematic diagram of the experimental arrangement of the stack used for the irradiation is shown in Fig. 1.

The irradiation for each sample was carried out for about 7–8 hours to build up sufficient activity, which was subsequently counted for an appropriate time by using a precali-
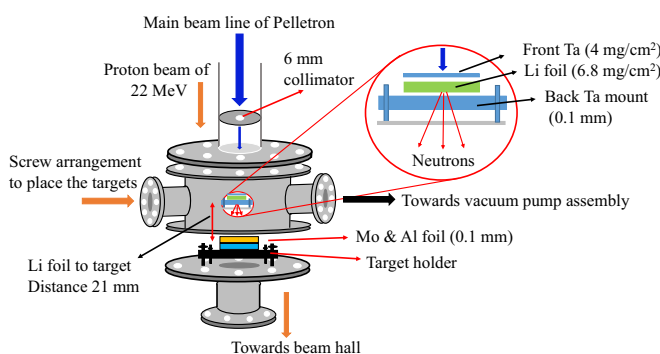

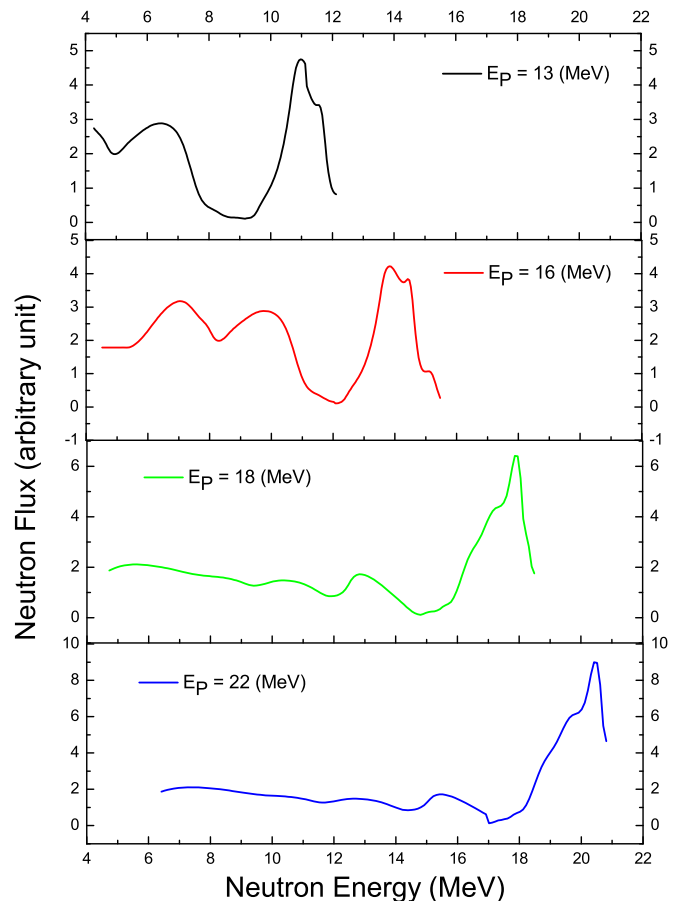FIG. 1. Schematic diagram of the experimental setup used for the irradiations.

FIG. 2. Neutron spectra generated from the $^{\text{nat}}\text{Li}(p, n)$ reaction using the four proton energies used for the irradiations

brated 80 cm^3 single-crystal high-purity germanium (HPGe) detector coupled to a PC based multichannel analyzer by placing them at a suitable distance from the end cap of the detector to avoid the pile-up effect. The HPGe detector was calibrated with a standard ^{152}Eu source. The resolution of the detector during counting was measured as 1.82 keV for 1332 keV of ^{60}Co. The dead time of the detector was kept below 2% throughout the counting of the samples.

III. DATA ANALYSIS

A. Calculations for neutron spectra

The proton energies 13, 16, 19, and 22 MeV were used in the present experiment for the irradiation purpose. The degradation of the protons in the Ta-Li-Ta stack was calculated using SRIM [42]. The proton beam energies at the center of the Li foil thickness were found to be 12.83 ± 0.11, 15.85 ± 0.08, 18.87 ± 0.07, and 21.88 ± 0.08 MeV, respectively. The neutron spectra for different proton energies are given in Fig. 2. A natural lithium foil was used to generate neutrons which consists of ^6Li and ^7Li isotopes with abundances of 7.42% and 92.58%, respectively [4]. A variety of reactions take place when the protons interact with the natural lithium target. The most prominent is the production of the ground state of ^7Be from the $^7\text{Li}(p, n)$ reaction, which has a threshold
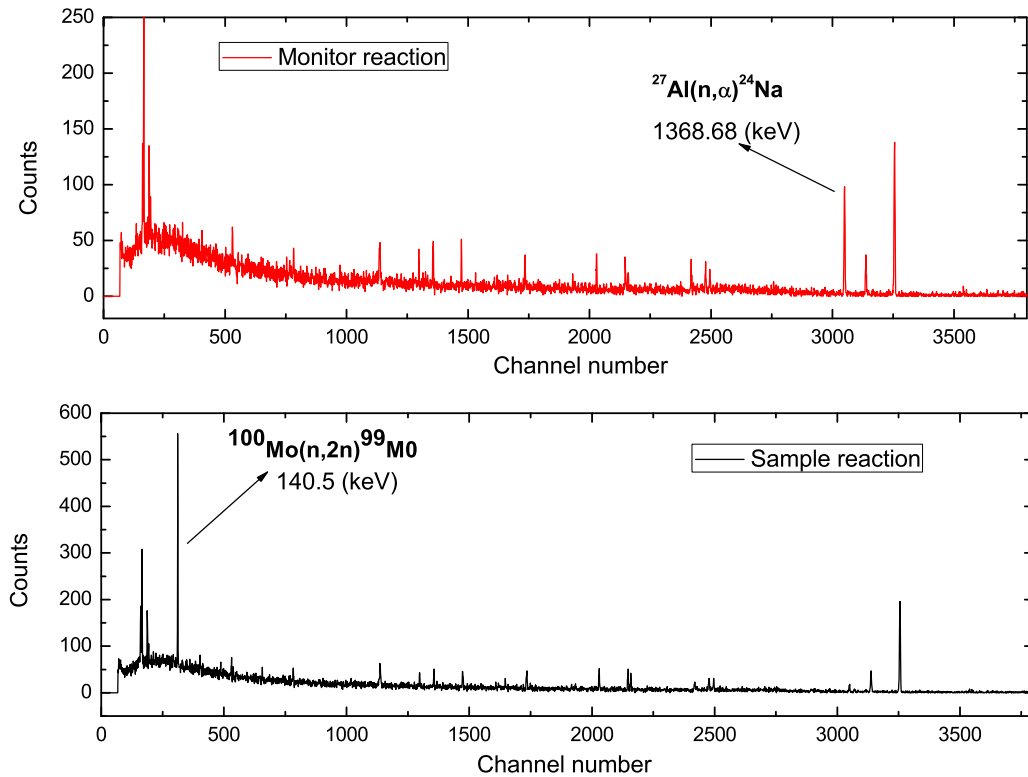
FIG. 3. The typically recorded spectra for the monitor and sample reactions.

energy of 1.88 MeV, whereas the threshold energy for its first excited state is 2.38 MeV. This reaction contributes to the main peak, as can be seen in Fig. 2. Above the proton energy of 2.38 MeV ($E_P > 2.4$ MeV), a second neutron group is produced due to the population of the first excited state of ^{7}Be. Therefore, solely from the population of the ground and the first excited states of ^{7}Be, two neutron groups n_0 and n_1 contribute to the neutron distribution. A detailed discussion on the generation of neutron spectra by using the branching ratios of the n_o and n_1 neutron groups by Poppe *et al.* [43] and the parametrization of the experimental neutron distributions by Meadows *et al.* [44] is provided in our earlier publication [23]. Due to contributions coming from different reaction channels, these neutron spectra have a quasi-monoenergetic peak near $E_P - 1.88$ MeV and a long continuum towards the lower energies, as shown in Fig. 2. This lower energy continuum is referred to as the tail region, consisting of lower neutron energies which also contribute in the reaction cross section. Therefore, it is necessary to remove the contribution arising from the tail part of the neutron spectrum. This correction can be done by considering spectral average cross sections [23,45] as described in the next section.

B. Measurement of ^{100}Mo($n, 2n$) reaction cross sections

The neutron spectra obtained by applying the methodology described above were used for the calculation of the neutron flux. In the present measurement, we used the ^{27}Al(n, α)^{24}Na ($E_{th} = 3.249$ MeV) reaction as the flux monitor. The typical γ spectrum recorded using the HPGe detector for the monitor reaction is shown in Fig. 3. The product ^{24}Na from this reaction has a prominent γ line of 1368.68 keV which has a half-life ($t_{1/2}$) of 14.997 ± 0.012 h [4]. The monitor reaction was chosen carefully, since its half-life is comparable to that of the ^{99}Mo isotope (65.976 ± 0.024 h) [4]. To obtain the flux value, a spectral weighted cross section ($\langle \sigma_W \rangle$) was first calculated for the monitor reaction using the evaluated cross sections taken from the ENDF-B/VII.1 [25] library, and also with the help of the relation

$$\langle \sigma_W \rangle = \frac{\sum_{E_i} \phi_i \sigma_i}{\sum_{E_i} \phi_i}, \tag{1}$$

where ϕ_i and σ_i are the neutron flux and corresponding monitor cross section respectively, taken from ENDF/B-VII.1 [25].

TABLE I. Nuclear spectroscopic properties for monitor and sample reactions taken from Ref. [4].

Reaction	Threshold (MeV)	$T_{1/2}$ (h)	Decay mode	E_γ (keV)	I_γ (%)
^{27}Al(n, α)^{24}Na	3.249	14.997 ± 0.012	β^- (100%)	1368.68	89.43 ± 0.23
^{100}Mo($n, 2n$)^{99}Mo	8.37	65.976 ± 0.024	β^- (100%)	140.5	9.9936 ± 0.0015

TABLE II. Measured and tailing corrected cross sections for the ^{100}Mo$(n, 2n)^{99}$Mo reaction.

Neutron energy	Flux	Cross section (mb)			
		Measured	Tailing part		Corrected
(MeV)	$(n\,cm^{-2}s^{-1})$		ENDF-B/VII.1	JENDL-4.0	
10.95 ± 0.45	7.27×10^5	1249.89	5.10	6.09	1243.89 ± 156.73
13.97 ± 0.68	1.48×10^6	1492.73	69.46	78.48	1422.53 ± 190.61
16.99 ± 0.53	2.68×10^6	1558.26	344.15	338.72	1216.82 ± 159.40
20.00 ± 0.58	3.09×10^6	1170.12	402.39	387.67	774.96 ± 98.41

The total neutron flux was calculated by using the expression

$$\langle\Phi\rangle = \frac{C_{obs}\lambda\left(\frac{CL}{LT}\right)}{N_0\langle\sigma_W\rangle I_\gamma \epsilon (1 - e^{-\lambda t_i})(e^{-\lambda t_c})(1 - e^{-\lambda LT})}, \quad (2)$$

where C_{obs} is the observed count for the considered γ ray from the monitor reaction, CL and LT are the clock time and the live time for the counting of the spectrum, λ is the decay constant ($\lambda = 0.693/t_{1/2}$), I_γ is the branching ratio for the considered γ ray taken from Ref. [4], N_0 is the total number of target nuclei in the sample, and ϵ is the detector efficiency. The spectroscopic data used in the calculation of flux are given in Table I. The monitor and the sample reactions have different threshold energies, 3.249 and 8.37 MeV, respectively. The sample reaction cross sections are not sensitive to neutrons below 8.37 MeV. However, the monitor reaction is sensitive to neutrons from 3.249 MeV to the maximum available energy. Therefore, the absolute neutron flux which contributes in the formation of ^{99}Mo was calculated by taking the area under the neutron distribution from threshold to maximum neutron energy for the sample reaction. Detailed methods for the flux correction have been described earlier [45].

A typical spectrum for the sample reaction with the γ lines used in the cross section measurement is shown in Fig. 3. The $(n, 2n)$ reaction channel for ^{100}Mo results in ^{99}Mo, which has a half-life of 65.976 ± 0.024 h. The $(n, 2n)$ reaction cross section was measured using the counting statistics of the decaying γ line of 140.5 (99.936 ± 0.0015) keV. Another reaction channel, ^{98}Mo$(n, \gamma)^{99}$Mo, is also responsible for the population of ^{99}Mo. Since both reaction channels result in the same product, the counts from the γ line were separated by taking the ratio R, using the method presented in Ref. [46],

$$R = C_{obs(n,2n)}/C_{obs(n,\gamma)} = \frac{a_{100}\sigma_{(n,2n)}}{a_{98}\sigma_{(n,\gamma)}}, \quad (3)$$

where a_{100} and a_{98} are the isotopic abundances of ^{100}Mo and ^{98}Mo, respectively. $\sigma_{(n,2n)}$ and $\sigma_{(n,\gamma)}$ are the ^{100}Mo$(n, 2n)^{99}$Mo

and ^{98}Mo$(n, \gamma)^{99}$Mo reaction cross-sections, which were calculated theoretically by using the model code TALYS-1.9 [28]. Equation (2) now can be rewritten for the calculation of reaction cross-section $\langle\sigma_R\rangle$ as

$$\langle\sigma_R\rangle = \frac{C_{obs}\lambda\left(\frac{CL}{LT}\right)}{N_0\langle\Phi\rangle I_\gamma \epsilon (1 - e^{-\lambda t_i})(e^{-\lambda t_c})(1 - e^{-\lambda LT})} \quad (4)$$

where σ_R is the reaction cross section, C_{obs} is the count from the $(n, 2n)$ channel only, and the other symbols have their same meanings as in Eq. (2). Neutron flux (Φ) calculated from Eq. (2) is used in (3). All the spectroscopic data for the calculations were taken from NuDat [4] and are given in Table I.

IV. COVARIANCE ANALYSIS

The covariance (correlation) analysis is a mathematical utility which provides the best estimation of the uncertainty along with the cross-correlations among the measured quantities, which in this case are the reaction cross sections. Besides the counts from the recorded spectra, the quantities which were used to calculate the cross-sections were taken from different sources and hence contain a significant amount of uncertainty in their values. Therefore, by using this technique, we are able to transfer these errors from all the sources into our final measured cross-section values. The counting of all the samples were done using the common detector setup. Therefore, all the measured cross sections are correlated with each other because of the detector efficiencies. In this method we first calculated the uncertainties in the detector efficiencies, then using those values we obtained the correlations among the cross sections.

The tailing corrected cross sections with the calculated uncertainties from the covariance analysis are given in Table II.

TABLE III. Co-variance matrix ($V_\varepsilon \times 100$) for the detector efficiency.

0.0030938					
0.0008305	0.0015126				
0.0005763	0.0003507	0.0009057			
0.0002955	0.0001798	0.0001248	0.0001840		
0.0002664	0.0001621	0.0001125	0.0000577	0.0001593	
0.0001346	0.0001346	0.000934	0.0000479	0.0000432	0.0000968

TABLE IV. Measured efficiencies with correlation matrix for the sample and the monitor reaction.

E_γ (KeV)	Efficiency	Correlation matrix	
140.5	0.089343 ± 0.001815	1	
1368.68	0.016874 ± 0.000287	0.348	1

A. Uncertainty in detector efficiency

The efficiency of the HPGe detector was determined by using the standard ^{152}Eu source. The absolute value of efficiency of a detector for different γ-ray energies is geometry dependent and is given by the relation

$$\varepsilon = K_c \frac{C}{N_0 I_\gamma e^{-\lambda T} \Delta t}, \qquad (5)$$

where ε is the geometry dependent efficiency and C is the observed count rate for a particular γ line of interest with absolute intensity I_γ. N_0 is the absolute disintegration rate for the ^{152}Eu sample at the time of manufacture and K_c are the summing correction factors calculated using the EFFTRAN code [47].

The detector efficiency can be expanded using a Taylor series as a function of four attributes, $\varepsilon = f(C, N_0, I_\gamma, t_{1/2})$:

$$\left(\frac{\Delta \varepsilon_i}{\varepsilon_i}\right)^2 = \left(\frac{\Delta C_i}{C_i}\right)^2 + \left(\frac{\Delta N_o}{N_0}\right)^2$$
$$+ \left(\frac{\Delta I_{\gamma_i}}{I_{\gamma_i}}\right)^2 + \left(T \ln 2 \frac{\Delta t_{1/2}}{t_{1/2}^2}\right)^2, \qquad (6)$$

where the terms have their usual definitions as stated in Refs. [48]. The covariance matrix for detector efficiencies can now be generated as

$$(V_\varepsilon)_{ij} = \sum_r e_{ir} S_{ijr} e_{jr}, \qquad (7)$$

where e_{ir}, e_{jr} are the diagonal matrices and S_{ijr} are the micro-correlation matrices, which may be given as an $(n \times n)$ unity matrix for the uncorrelated elements and an $(n \times n)$ square matrix with each element as "1" for the completely correlated case. S_{ijr} can also be an $(n \times n)$ matrix with elements $0 < S_{ijr} < 1$ for partial correlated cases. The microcorrelation
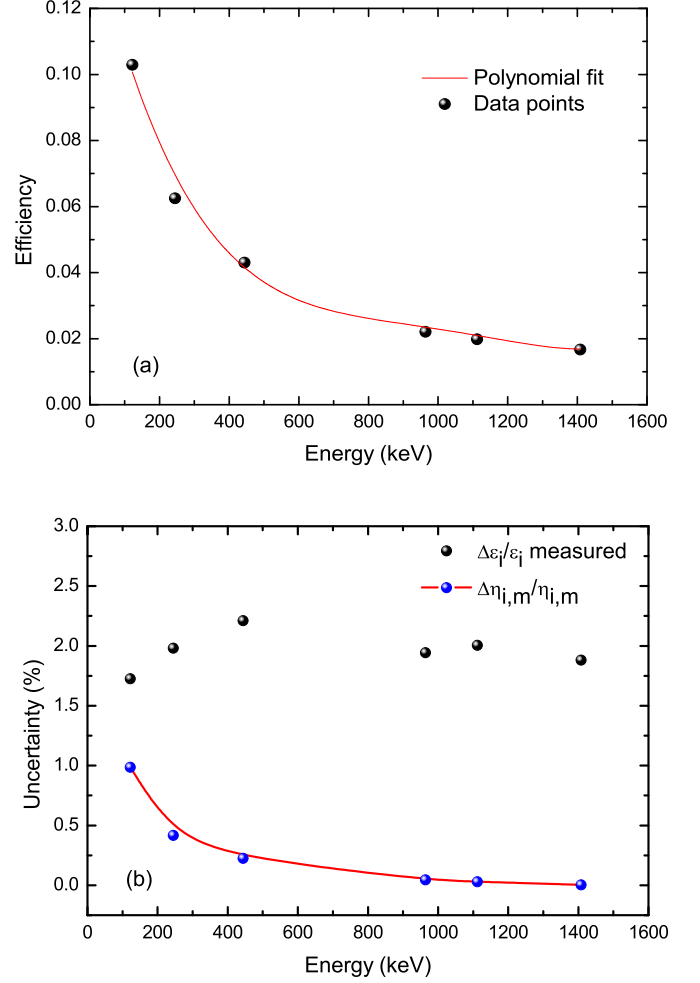

FIG. 4. (a) Measured detector efficiency and (b) the comparison of measured uncertainty in efficiencies ($\Delta\varepsilon_i/\varepsilon_i$) with the uncertainty in the detector efficiencies relative to the monitor efficiency ($\Delta\eta_{i,m}/\eta_{i,m}$)

matrices for $(C, N_0, I_\gamma, T_{1/2})$ can be given as

$$\begin{bmatrix} 1 & 0 & 0 \\ 0 & 1 & 0 \\ 0 & 0 & 1 \end{bmatrix}, \begin{bmatrix} 1 & 1 & 1 \\ 1 & 1 & 1 \\ 1 & 1 & 1 \end{bmatrix}, \begin{bmatrix} 1 & 0 & 0 \\ 0 & 1 & 0 \\ 0 & 0 & 1 \end{bmatrix},$$

$$\text{and} \begin{bmatrix} 1 & 1 & 1 \\ 1 & 1 & 1 \\ 1 & 1 & 1 \end{bmatrix}.$$

TABLE V. Fractional uncertainties in various parameters used to obtain ^{100}Mo$(n, 2n)^{99}$Mo cross sections.

E_n (MeV)	Partial uncertainty (%)												
	C_s	C_m	$I_{\gamma s}$	$I_{\gamma m}$	$\eta_{m,s}$	$f_{\lambda s}$	$f_{\lambda m}$	M_s	M_m	a_s	A_s	A_m	σ_W
10.95 ± 0.45	8.687	8.152	0.257	0.002	0.919	0.035	0.078	1.996	1.884	3.157	0.010	2.59×10^{-6}	0.973
13.97 ± 0.68	10.591	6.949	0.257	0.002	0.919	0.036	0.078	1.970	2.026	3.157	0.010	2.59×10^{-6}	0.462
16.99 ± 0.53	7.213	10.161	0.257	0.002	0.919	0.036	0.075	1.981	1.823	3.157	0.010	2.59×10^{-6}	0.826
20.00 ± 0.58	8.025	8.908	0.257	0.002	0.919	0.036	0.079	1.931	1.879	3.157	0.010	2.59×10^{-6}	1.301
Corr	0	0	1	1	1	1	1	0	0	1	1	1	0

TABLE VI. Covariance matrix (%) and corresponding correlation coefficients for the measured ^{100}Mo($n, 2n$)^{99}Mo cross sections.

E_n (MeV)	Covariance matrix ($V_{cs_{ij}}$)				Correlation matrix			
10.95 ± 0.45	1.611726				1			
13.97 ± 0.68	0.108844	1.795559			0.064	1		
16.99 ± 0.53	0.108842	0.108842	1.740994		0.065	0.061	1	
20.00 ± 0.58	0.108845	0.108846	0.108843	1.635372	0.067	0.063	0.064	1

The covariance matrix generated using Eqs. (5) and (6) is given in Table III. The efficiencies and the relative correlations were generated using the model equation

$$\ln \varepsilon_i = \sum_m p_m (\ln E_i)^{m-1}, \quad (8)$$

where ε_i are the efficiencies considered in the cross section calculations, p_m are the fitting parameters of order m, and E_i are the corresponding γ-ray energies. Equation (7) can be written as $Z = AP$, with fitting parameters $\hat{P}$ given as

$$\hat{P} = V_{\hat{P}} \left(A' V_z^{-1} Z \right), \quad (9)$$

where matrix V_z can be obtained using $(V_z)_{ij} = \frac{(V_\epsilon)_{ij}}{\langle \epsilon_i \rangle \langle \epsilon_j \rangle}$, $V_{\hat{P}}$ is the covariance matrix, and the goodness of the fit can be calculated by $\chi^2_m = (Z - AP)' V_z^{-1} (Z - AP)$ [48]. Using Eq. (8) we obtain the fitting parameters as $\hat{P} = (-0.38370, -0.8694, 0.1693, 0.3208, -0.1)$ with a value of $\chi^2_m = 0.72$. The calculated efficiencies and the corresponding correlation matrix for characteristic γ lines 140.5 and 1368.68 keV, using $\hat{P}$ and $V_{\hat{P}}$, are given in Table IV.

B. Uncertainty in the cross section measurement

The sample reaction cross sections $\langle \sigma_s \rangle$ were normalized with respect to the monitor reaction cross sections $\langle \sigma_m \rangle$, therefore the ratio measurement technique [49] was used to generate the covariance matrix utilizing the uncertainty of

each parameter. The sample reaction parameters are denoted with subscript s and the monitor reaction parameters with subscript m. Using Eqs. (2) and (3), we can write

$$\langle \sigma_s \rangle = \langle \sigma_m \rangle \frac{C_s N_{0_m} \varepsilon_m I_{\gamma_m} f_{\lambda_m}}{C_m N_{0_s} \varepsilon_s I_{\gamma_s} f_{\lambda_s}} \quad (10)$$

with the time factor f defined as

$$f = (1 - e^{-\lambda t_i})(e^{-\lambda t_c})(1 - e^{-\lambda LT})/\lambda. \quad (11)$$

Using the number of target nuclei N_0 [given by $N_0 = (M N_A a)/A$, where M is the sample weight, N_A is the Avogadro number, a is the isotopic abundance, and A is atomic mass), Eq. (9) becomes

$$\langle \sigma_s \rangle = \langle \sigma_m \rangle \frac{C_s M_m a_m A_s \varepsilon_m I_{\gamma_m} f_{\lambda_m}}{C_m C_s M_s a_s A_m \varepsilon_s I_{\gamma_s} f_{\lambda_s}} \quad (12)$$

The partial uncertainties due to each attribute in the above equation can be propagated directly to the sample cross section $\langle \sigma_s \rangle$ using the quadratic sum formula, except the decay constant which is related to $\langle \sigma_s \rangle$ by an exponential function; therefore, the uncertainty in the time factor f must be propagated as

$$\left(\frac{\Delta f}{f} \right)^2 = \left(\frac{\lambda t_i e^{-\lambda t_i}}{1 - e^{-\lambda t_i}} - \lambda t_c + \frac{\lambda(LT) e^{-\lambda(LT)}}{1 - e^{-\lambda(LT)}} - 1 \right)^2 \left(\frac{\Delta \lambda}{\lambda} \right)^2. \quad (13)$$
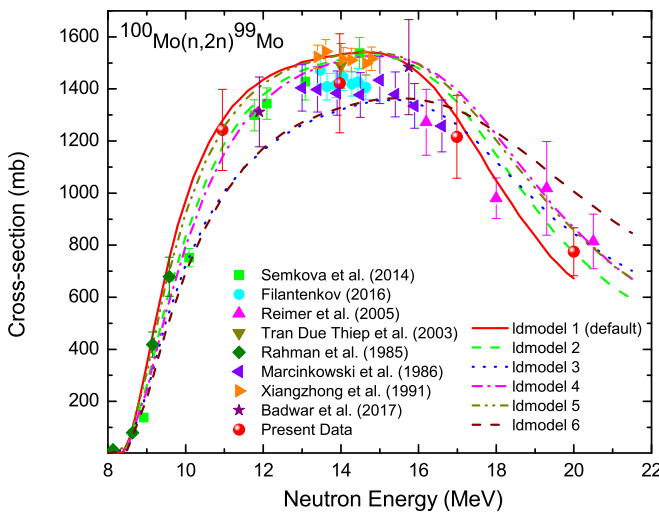

FIG. 5. A comparison of the present experimental ^{100}Mo($n, 2n$)^{99}Mo reaction cross sections with the literature data [13–22], and with the theoretical values from different ldmodels in TALYS-1.9 [28].

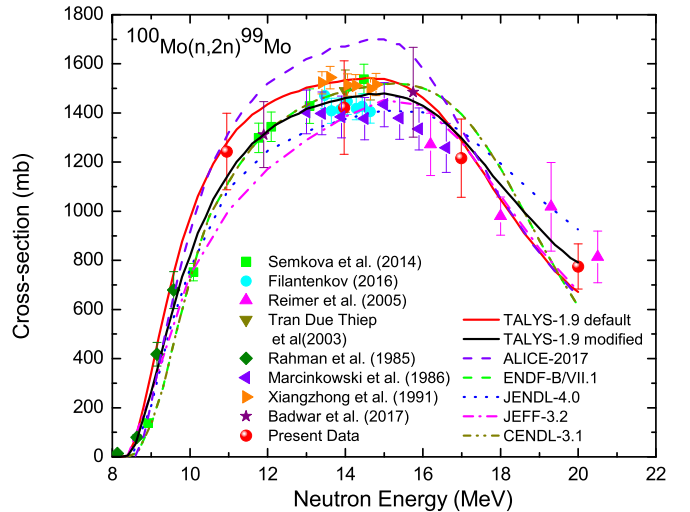FIG. 6. A comparison of the present experimental ^{100}Mo($n, 2n$)^{99}Mo reaction cross sections with the literature data [13–22], the evaluated data [24–27], ALICE-2017 [29], and the theoretical values using optimized parameters in TALYS-1.9 [28].

TABLE VII. Default and adjusted parameters used in the TALYS-1.9 calculations.

Parameter	CTM default	CTM adjusted
α	0.06926	0.03974
β	0.28269	0.28269
γ_1	0.4331	0.04331

The uncertainty in the detector efficiencies can be reduced further for both the sample and the monitor by introducing $\eta_{m,s} = \varepsilon_m/\varepsilon_s$ [49] with the partial uncertainty given as $\frac{\Delta\eta_{m,s}}{\eta_{m,s}} = \mathrm{var}(\varepsilon_m) + \mathrm{var}(\varepsilon_s) - 2\,\mathrm{cov}(\varepsilon_m, \varepsilon_s)$. For visualization, the measured detector efficiencies ε_i, the fractional uncertainty (%) in the measured efficiencies, and the uncertainty (%) of the $\eta_{i,m}$ values are shown in Fig. 4. It is very clear from the Fig. 4 that the uncertainties in the measured efficiencies become $<1\%$ after taking the ratio $\eta_{i,m}$. Using a similar approach, the $\frac{\Delta\eta_{m,s}}{\eta_{m,s}}$ value was found to be only 0.919% for the sample-to-monitor ratio. The microcorrelation matrix for the efficiency can now be given as the (4×4) matrix containing each element as 0.919. The partial uncertainties for each element of Eq. (11) along with their correlations among the four neutron energies are given in Table V. We have omitted the isotopic abundance for the monitor reaction as ^{27}Al has 100% isotopic abundance [4]. The covariance matrix (V_{cs}) for the reaction cross sections at four neutron energies are given in Table VI. Similarly, the correlation matrix generated by using Eq. (6) based on the above assumptions are also given in Table VI. The uncertainty (%) in each cross-section value can now be calculated by simply considering the $\sqrt{(V_{cs})_{ij}}$ for the respective diagonal element of the covariance matrix.

V. THEORETICAL FRAMEWORK

A. Calculations using the TALYS-1.9 code

TALYS-1.9 [28] is a nuclear model code which is used to reproduce different nuclear reactions including neutron, photon, proton, deuteron, triton, ^{3}He, and α particles as pro-
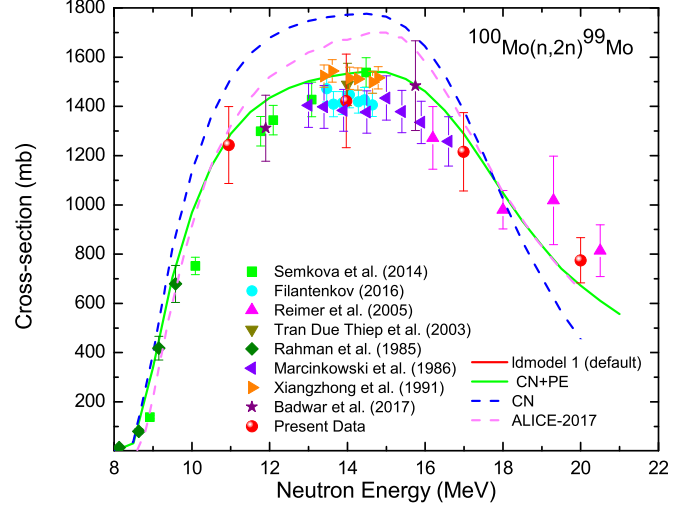

FIG. 7. A comparison of the experimental ^{100}Mo$(n, 2n)^{99}$Mo reaction cross sections with the theoretical values using CN and CN+PE modes in TALYS-1.9 [28].

jectiles on target nuclei for incident energies up to 200 MeV. The TALYS model code uses the reaction parameters from the Reference Input Parameter Library (RIPL) database [50]. The code accounts for the effect of level density parameters, compound, pre-equilibrium, and direct reaction mechanisms as a function of the incident particle energy. The optical model parameters were obtained by using a global potential, proposed by Koning and Delaroche [51]. The compound nucleus reaction mechanism have been incorporated by using the Hauser-Feshbach model [52]. The pre-equilibrium contribution has been accounted for by an exciton model which was developed by Kalbach [53]. In the present work, we have calculated the ^{100}Mo$(n, 2n)^{99}$Mo reaction cross sections for neutron energies of 10.95 ± 0.45, 13.97 ± 0.68, 16.99 ± 0.53, and 20.00 ± 0.58 MeV by using the default and the adjusted input parameters in the TALYS-1.9 model code. It includes all the possible outgoing reaction channels for a particularly chosen projectile + target system. There are six

TABLE VIII. Systematic formulas proposed by different authors for the (n, p) reaction.

Author	Formula for $\sigma_{n,p}$	Mass region	n	Ref.
Levkovski	$\sigma_{n,p} = 50.21(A^{1/3} + 1)^2 \exp\left(-\frac{33.80(N-Z)}{A}\right)$	$40 \leqslant A \leqslant 209$	94	[30]
Ait-Tahar	$\sigma_{n,p} = 90.68(A^{1/3} + 1)^2 \exp\left(-\frac{34.48(N-Z+1)}{A}\right)$	$40 \leqslant A \leqslant 187$	86	[31]
Kasugai	$\sigma_{n,p} = 1264(N - Z + 1) \exp\left(-\frac{46.63(N-Z+1)}{A}\right)$	$28 \leqslant A \leqslant 187$	89	[32]
Doczi	$\sigma_{n,p} = 18.12(A^{1/3} + 1)^2 \exp\left(-19.61\frac{(N-Z)}{A} + \frac{(N-Z)^2}{A^2}\right)$	$28 \leqslant A \leqslant 209$	100	[33]
Forrest	$\sigma_{n,p} = 900(A^{1/3} + 1)^2 \exp\left(-49.27\frac{(N-Z)}{A} + 197.1\frac{(N-Z)^2}{A^2} - 0.45A^{1/2}\right)$	$40 \leqslant A \leqslant 187$	186	[34]
Bychkov	$\sigma_{n,p} = 7.06\pi r_0^2(A^{1/3} + 1)^2 \exp\sqrt{\frac{a}{E_n}}\left(\frac{0.58(Z-1)}{A^{1/3}} - \frac{50(N-Z+1)}{A} - 3.26\right)$	$28 \leqslant A \leqslant 209$	100	[35]
Luo	$\sigma_{n,p} = 62.98(A^{1/3} + 1)^2 \exp\left(-34.45\frac{(N-Z)}{A}\right)$	$46 \leqslant A \leqslant 196$	36	[36]
Habbani	$\sigma_{n,p} = 60.34(A^{1/3} + 1)^2 \exp\left(-34.44\frac{(N-Z+1)}{A}\right)$	$28 \leqslant A \leqslant 208$ (even A)	23	[37]
	$\sigma_{n,p} = 20.91(A^{1/3} + 1)^2 \exp\left(-29.53\frac{(N-Z)}{A}\right)$	$29 \leqslant A \leqslant 209$ (odd A)	13	

TABLE IX. Systematic formulas proposed by different authors for the $(n, 2n)$ reaction.

Author	Formula for $\sigma_{n,2n}$	Mass region	n	Ref.
Chatterjee	$\sigma_{n,2n} = 31.39(A^{1/3} + 1)^2 \exp\left(\frac{1.706(N-Z)}{A}\right)$	$45 \leqslant A \leqslant 238$	49	[38]
Lu and Fink	$\sigma_{n,2n} = 45.76(A^{1/3} + 1)^2[1 - 7.372\exp\left(-\frac{32.21(N-Z+1)}{A}\right)]$	$28 \leqslant Z \leqslant 82$	45	[39]
Luo	$\sigma_{n,2n} = 0.0226(A^{1/3} + 1)^2 \exp\left(\frac{133.86(N-Z)}{A} - \frac{779.47(N-Z)^2}{A^2} + \frac{1500.51(N-Z)^3}{A^3}\right)$	$23 \leqslant A \leqslant 209$	50	[36]
Bychkov	$\sigma_{n,2n} = 8.7(A + 100)[1 - 0.88\exp\left(-\frac{7.95(N-Z)}{A}\right)]$	$45 \leqslant A \leqslant 238$	49	[35]
Habbani	$\sigma_{n,2n} = 23.53(A^{1/3} + 1)^2 \exp\left(3.50\frac{(N-Z)}{A}\right)$	$45 \leqslant A \leqslant 209$ (odd A)	10	[37]
	$\sigma_{n,2n} = 20.82(A^{1/3} + 1)^2 \exp\left(3.76\frac{(N-Z+1)}{A}\right)$	$48 \leqslant A \leqslant 238$ (even A)	39	

level density models (ldmodels) incorporated in this model code for a better description of the nuclear data. The different level densities in the TALYS code (ldmodels 1–6) account for the constant-temperature Fermi gas model (CTFGM) [54], back-shifted Fermi gas model (BSFGM) [55], generalized superfluid model (GSFM) [56,57], microscopic level densities from Goriely's and Hilaire's tables [58], and microscopic level densities (temperature-dependent HFB, Gogny force) [59], respectively. Each ldmodel was used for the reproduction of the measured data. A comparison of the present and the literature data is provided in Fig. 5. Furthermore, the input level density parameters were adjusted to get a better description of the results. The TALYS-1.9 code uses the effective constant-temperature model (CTM), introduced by Gilbert and Cameron [34], as default to perform the simulations. The CTM divides the excitation energy into two parts: first the lower energy part from minimum excitation energy to a matching energy E_M, where the constant temperature laws apply, and the second above E_M, where the Fermi gas model applies. The nuclear level density (a) in general form can be written as

$$a = \tilde{a}\left[1 + \delta\varepsilon_0\left(\frac{1 - \exp[-\gamma(E_x - \Delta)]}{(E_x - \Delta)}\right)\right], \quad (14)$$

$$\tilde{a} = \alpha A + \beta A^{2/3}, \quad \gamma = \frac{\gamma_1}{A^{1/3}} + \gamma_2, \quad (15)$$

where, the symbols have their usual meanings as given in Refs. [23]. By changing the values of $\tilde{a}$, a better fit was found for the plotted data in Fig. 6, and the values of the used parameters are given in Table VII. It can be seen from Fig. 6 that the TALYS-1.9 default values are slightly higher for the neutron energy range from threshold to 17 MeV; however, it drastically decreases above this energy. The adjusted parameters were found to reproduce the cross-section values to an acceptable degree, for the entire range of neutron energies under consideration.

B. Calculations using the ALICE-2017 code

The ALICE-2017 [29] is also another nuclear model code based on the Monte Carlo approach to perform theoretical calculations for the nuclear reactions using the projectiles γ, n, p, α or heavy-ions within the incident energy range 0.2–250 MeV. We have used the Obninsk level density [29] to simulate the ^{100}Mo$(n, 2n)^{99}$Mo reaction cross sections from threshold to 20 MeV. The Obninsk level density [29] option is an interesting case to investigate the validation of this code for fast-neutron-induced reactions. The cross sections calculated using ALICE were found to be in a good agreement with experimental data and the TALYS-1.9 code (default) except for the neutron energies within 11 to 17 MeV as shown in Fig. 6.

TABLE X. Systematic formulas proposed by different authors for the (n, α) reaction.

Author	Formula for $\sigma_{n,\alpha}$	Mass region	n	Ref.
Levkovski	$\sigma_{n,\alpha} = 16.55(A^{1/3} + 1)^2 \exp\left(-\frac{31.26(N-Z)}{A}\right)$	$31 \leqslant A \leqslant 202$	12	[30]
Ait-Tahar	$\sigma_{n,\alpha} = 31.66(A^{1/3} + 1)^2 \exp\left(-\frac{32.75(N-Z+1)}{A}\right)$	$40 \leqslant A \leqslant 188$	12	[31]
Kasugai	$\sigma_{n,\alpha} = 277.86 \exp\left(-\frac{24.66(N-Z)}{A}\right)$	$19 \leqslant A \leqslant 187$	12	[32]
Konobeyev	$\sigma_{n,\alpha} = 53.066(A^{1/3} + 1)^2 \exp\left(-209.11S^2 + 8.4723P - 0.19253Z/A^{1/3} - 0.96249)\right),$	$40 \leqslant A \leqslant 209$	7	[40]
	$Z \leqslant 50$			
	$\sigma_{n,\alpha} = 53.066(A^{1/3} + 1)^2(-1.6462P + 0.39951)^3, Z > 50$	$40 \leqslant A \leqslant 209$	6	
	$S = (N - Z + 1)/A, P = (N - Z + 09.5)/A$			
Forrest	$\sigma_{n,\alpha} = 24.71(A^{1/3} + 1)^2 \exp\left(-19.77\frac{(N-Z)}{A} + 13.82\frac{(N-Z)^2}{A^2} - 0.0248A\right)$	$20 \leqslant Z \leqslant 50$	7	[34]
Luo	$\sigma_{n,\alpha} = 20.91(A^{1/3} + 1)^2 \exp\left(-34.69\frac{(N-Z)}{A}\right)$	$50 \leqslant A \leqslant 206$	13	[36]
Habbani	$\sigma_{n,\alpha} = 3.6(A^{1/3} + 1)^2 \exp\left(-25\frac{(N-Z-3)}{A}\right)$	$26 \leqslant A \leqslant 238$ (even A)	7	[37]

TABLE XI. Calculated (n, p) cross sections using the systematic formulas given in Table VIII.

A	$\sigma_{n,p}$ (mb) around 14.5 MeV								
	Levkovski	Ait-Tahar	Kasugai	Doczi	Forrest	Bychkov	Luo	Habbani	EXFOR data
92	80.79	94.54	118.82	86.33	22.35	5.41	95.76	63.15	72.0 ± 3.0
94	42.39	49.35	59.34	55.44	17.38	2.12	49.62	32.99	54.3 ± 5.4
95	31.02	36.02	41.97	44.51	16.22	1.34	36.09	21.18	41.0 ± 5.5
96	22.86	26.47	29.74	35.78	15.68	0.86	26.43	17.71	25.6 ± 0.8
97	16.94	19.58	21.14	28.80	15.66	0.56	19.48	12.51	16.67 ± 1.20
98	12.64	14.57	15.07	23.21	16.13	0.36	14.45	9.76	5.3 ± 0.5
100	7.16	8.22	7.75	15.15	18.64	0.16	8.09	5.50	6.2 ± 1.4

C. Calculations using different systematic formulas for the (n, p), $(n, 2n)$, and (n, α) reactions

A large number of systematic formulas have been proposed over the years to calculate the (n, p), $(n, 2n)$, and (n, α) reaction cross sections at 14.5 MeV for advanced reactor design, for medical accelerators, and for the development of the International Thermonuclear Experimental Reactor (ITER). In order to provide a thorough study of the present case, we have calculated all the possible primary neutron induced reaction cross sections by using the systematic formulas given by several authors [30–40]. The systematic formulas for the (n, p), $(n, 2n)$, and (n, α) reactions are given in Tables VIII, IX, and X, respectively. The reaction cross sections were calculated using the given formulas and are listed in Tables XI, XII, and XIII, respectively for the comparison of (n, p), $(n, 2n)$, and (n, α) reaction cross sections measured at 14.5 MeV, taken from the EXFOR database [12]. The present compilation also serves the purpose of validating these systematics using the literature data.

VI. RESULTS AND DISCUSSIONS

The ^{100}Mo$(n, 2n)^{99}$Mo reaction cross sections were measured using the offline γ-ray spectroscopic measurement technique. The ^{27}Al$(n, \alpha)^{24}$Na reaction was used for monitoring the neutron flux. The uncertainties in the measurement was calculated using covariance analysis. The measured data are compared with the evaluated data libraries ENDF-B/VII.1 [24], JENDL-4.0 [25], JEFF-3.2 [26], and CENDL-3.1 [27]. The present data are also compared with the theoretical model codes TALYS-1.9 [28] and ALICE-2017 [29]. The present experimental results along with the evaluated data taken from ENDF-B/VII.1 [24] and JENDL-4.0 [25] are given in Table II.

The comparison of the data with the theoretically reproduced cross sections using the different ldmodels in the TALYS-1.9 model code [28] are shown in Fig. 5. It can be

observed from the figure that each of the ldmodels successfully produced the trend of the cross-section data, except for ldmodel 6 [59]. However, the present data can be described in a suitable manner with the modified input parameters of any of the ldmodels present in the TALYS-1.9 model code [28]. Therefore, we have made an effort to find a better fit for the data presented in Fig. 6 by modifying the input data set for the ldmodel 1 [54], which is used by the TALYS-1.9 code [28] as default. The modified set of parameters is given in Table VII. From Fig. 6, it can be observed that the present results show a better agreement with the data measured by others [13–21] using the D+T or D+D reactions and by Sylvia *et al.* [22] using ^{7}Li(p, n) reaction as the neutron generator. It can also be observed from the figure that the evaluated cross sections from different data libraries have a remarkable variation within the range of the measurement. However, the measured cross sections were found to be in consensus with the literature data [13–22].

The ALICE-2017 code [29] was also used by invoking the Obninsk level density [29] parameter to check the validation of the code in the present measurement. Primarily, the ALICE-2017 code has been used and found suitable for the reproduction of the heavy-ion induced reaction cross sections. The theoretical cross sections from the ALICE-2017 model code [29] were found to be in good agreement with the measured as well as the evaluated data for neutron energies lower than 11 MeV; however, the cross-section values around the peak are larger then the TALYS-1.9 [28] results. This small enhancement in the cross-section values around the peak may be due to the overprediction of the compound nucleus (CN) contribution using ALICE-2017. A similar trend can be observed in Fig. 7, where the reaction cross sections were reproduced for pure CN and with the pre-equilibrium (PE) contribution. It can be observed that TALYS-1.9 [28] is also overpredicting the CN contribution in the formation of the reaction residue. However, the lower values of experimental data suggest that the major contribution is coming from the direct reactions

TABLE XII. Calculated $(n, 2n)$ cross sections using the systematic formulas given in Table IX.

A	$\sigma_{n,2n}$ (mb) around 14.5 MeV						Present data at 13.97 MeV
	Chatterjee	Lu and Fink	Luo	Bychkov	Habbani	EXFOR data	
94	1157.98	1070.62	955.40	1050.27	994.63		
100	1312.62	1394.38	1451.00	1310.85	1255.70	1503 ± 45	1422.30 ± 190.61

TABLE XIII. Calculated (n, α) cross sections using the systematic formulas given in Table X.

A	$\sigma_{n,\alpha}$ (mb) around 14.5 MeV							
	Levkovski	Ait-Tahar	Kasugai	Konobeyev	Forrest	Luo	Habbani	EXFOR data
92	33.21	39.09	26.69	30.39	15.27	31.14	28.13	33.5 ± 2.4
98	5.99	6.63	6.73	2.88	5.39	4.64	6.85	6.56 ± 0.39
100	3.54	3.85	4.41	1.09	3.97	2.59	4.44	2.7 ± 0.3

in the formation of the reaction product, as no significant contribution has been observed from the PE process.

To have a better understanding of the neutron-induced reactions on Mo, we have calculated the cross section for all the possible channels using the systematic formulas proposed by different authors [30–40] and compared them with the experimental data taken from the EXFOR database [12] at 14.5 MeV. The calculated cross sections are listed in Tables XI, XII, and XIII for the (n, p), $(n, 2n)$, and (n, α) reactions respectively. The (n, p) reaction on the Mo isotopes [^{A}Mo$(n, p)^A$Nb] results in Nb residues for a particular mass number A. The calculated results are compiled in Table XI along with the EXFOR data. It can be observed from Table XI that the calculated cross sections using systematics proposed by different authors are in agreement with each other and were found to be successful in reproducing the data, except for the calculated results from Forrest [34] and Bychkov [35]. However, the results from Kasugai [32] and Luo [36] were found to be closest to the experimental data from EXFOR [12]. The possible $(n, 2n)$ reaction in Mo isotopes are ^{94}Mo$(n, 2n)^{93}$Mo and ^{100}Mo$(n, 2n)^{99}$Mo. The $(n, 2n)$ reactions for all the other Mo isotopes result in stable Mo isotopes. The calculated data for the $(n, 2n)$ reaction are given in Table XII. It can be observed that the present results as well as the EXFOR [12] data were also found to be in agreement with the model calculations. Furthermore, in the case of the (n, α) reaction, there are three Mo isotopes that produces Zr residue. The calculated data are tabulated in Table XIII. The systematic formulas given in Table IX for the (n, α) reactions were found to be satisfactory for the reproduction of the literature data to an acceptable degree.

VII. CONCLUSIONS

The ^{100}Mo$(n, 2n)^{99}$Mo reaction cross sections for the average neutron energies of 10.95 ± 0.45, 13.97 ± 0.68, 16.99 ± 0.53 and 20.00 ± 0.58 MeV were measured. The uncertainties in the measured data were calculated using covariance

analysis and they were found to be within the range 12–18%. The measured data were compared with theoretical model codes TALYS-1.9 and ALICE-2017, and with different evaluated data libraries, ENDF/B-VII.1, JENDL-4.0, JEFF-3.1, and CENDL-3.2. A modified input parameter set was introduced to the TALYS-1.9 model code to achieve a perfect fitting of the present measurement and the data available in EXFOR. The ALICE-2017 calculated values were found to be little enhanced around the neutron energies of 11–17 MeV. However, the TALYS-1.9 (modified) results together with ENDF/B-VII.1 and CENDL-3.1 were found to be suitable for the reproduction of the measured data for the present system. A systematic compilation was also performed using the theoretical formulas from different authors. The calculated results were found to be in good agreement with the measured values taken from the EXFOR database. In the present work, the systematic formulas and the ALICE-2017 model code were found to be adequate for the reproduction of the cross-section data. The present work also offers a better insight into the theoretical model code TALYS-1.9. It can also be stated that the production of such experimental data is also vital for medium to fast neutron energies to test different nuclear model codes and for the advancement of modern nuclear reactor technology and medical accelerators.

[1] C. Rubbia, J. A. Rubio, S. Buono, F. Carminati, N. Fiétier, J. Galvez, C. Gelès, Y. Kadi, R. Klapisch, P. Mandrilion, J. P. Revol, and Ch. Roche, Conceptual Design of a Fast Neutron Operated High Power Energy Amplifier, CERN Report No. CERN/AT/95-44 (ET), 1995, http://cds.cern.ch/record/289551/files/cer-0210391.pdf.

[2] C. D. Bowman, Annu. Rev. Nucl. Part. Sci. **48**, 505 (1998).

[3] P. Reimer *et al.*, Phys. Rev. C **71**, 044617 (2005).

[4] NuDat 2.7β, 2011, National Nuclear Data Center, Brookhaven National Laboratory, http://www.nndc.bnl.gov/

[5] T. Ruth, Nature (London) **457**, 536 (2009).

[6] *International Atomic Energy Agency, Nuclear Technology Review, Annex VIII: Production and Supply of Molybdenum-99 (2008)* (IAEA/NTR, Vienna, 2010), pp. 50–167.

[7] National Research Council, *Medical Isotope Production Without Enriched Uranium* (National Academies Press, Washington, 2009), Appendix D.

[8] K. Gagnon *et al.*, J. Nucl. Med. Biol. **38**, 907 (2011).

[9] S. Takacs *et al.*, J. Radioanal. Nucl. Chem **257**, 195 (2003).

[10] M. C. Lagunas-Solar *et al.*, Am. Nucl. Soc. **74**, 134 (1996).

[11] H. Naik *et al.*, J. Radioanal. Nucl. Chem. **295**, 807 (2013).

[12] EXFOR, NDS-120, 272–276, 2014, https://www-nds.iaea.org/exfor/exfor.htm

[13] Y. Ikeda *et al.*, JAERI Rep. **1312** (1988).

[14] A. A. Filatenkov *et al.*, Khlopin Radiev. Inst. Report No. 252, 1991 (unpublished).

[15] A. A. Filatenkov *et al.*, Khlopin Radiev. Inst. Report No. 258, 1999, https://www-nds.iaea.org/publications/indc/indc-ccp-0402/.

[16] M. M. Rahman and S. M. Qaim, Nucl. Phys. A **435**, 43 (1985).

[17] A. Marcinkowski *et al.*, Z. Phys. A - Atomic Nuclei **323**, 91 (1986).

[18] K. Xiangzhong *et al.*, High Energy Phys. Nucl. Phys. **15**, 549 (1991) (Chinese edition).

[19] A. A. Filatenkov, USSR Report to the INDC, No. 0460, 2016, https://www-nds.iaea.org/publications/indc/indc-ccp-0460/.

[20] T. D. Thiep *et al.*, Nucl. Phys. A **722**, C568 (2003).

[21] V. Semkova and R. Nolte, EPJ Web Conf. **66**, 03077 (2014).

[22] S. Badwar *et al.*, Appl. Radiat. Isot. **129**, 117 (2017).

[23] S. Parashari *et al.*, Phys. Rev. C **98**, 014625 (2018).

[24] M. B. Chadwick *et al.*, Nucl. Data Sheets **112**, 2887 (2011).

[25] K. Shibata *et al.*, J. Nucl. Sci. Technol. **48**, 429 (2011).

[26] A. J. Koning *et al.*, J. Kor. Phys. Soc. **59**, 1057 (2011).

[27] Z. G. Ge *et al.*, J. Kor. Phys. Soc. **59**, 1052 (2011).

[28] A. J. Koning, S. Hilaire, and S. Goriely, *TALYS User Manual: A Nuclear Reaction Program*, NRG-1755 (Nuclear Research and Consultancy Group, Petten, The Netherlands, 2015).

[29] M. Blann, Phys. Rev. C **54**, 1341 (1996).

[30] V. N. Levkovski, Zh. Eksp. Teor. Fiz. **45**, 305 (1963).

[31] S. Ait-Tahar, J. Phys. G: Nucl. Phys. **13**, L121 (1987).

[32] Y. Kasugai, Y. Ikeda, H. Yamamito, and K. Kawade, in *Proceedings of the 1994 Symposium on Nuclear Data, November 1994, Tokai, Japan* (JAERI, Ibaraki, 1995), https://inis.iaea.org/collection/NCLCollectionStore/_Public/27/038/27038623.pdf?r=1&r=1.

[33] R. Doczi, V. Semkova, A. D. Majdeddin, C. M. Buczko, and J. Csikai, IAEA-NDS Report No. Indc(HUN)-032, 1997, https://www-nds.iaea.org/publications/indc/indc-hun-0032/.

[34] R. A. Forrest, Report AERE-R-12149. Atomic Energy Research Establishment, Harwell, https://inis.iaea.org/search/search.aspx?orig_q=RN:18063795.

[35] V. M. Bychkov, V. N. Manokhin, A. B. Pashchenko, V. I. Plyashin, IAEA-NDS Report No. Indc(CCP) 146, 1980, https://www-nds.iaea.org/publications/indc/indc-ccp-0146/.

[36] J. Luo *et al.*, Nucl. Instrum. Method Phys. Res. B **266**, 4862 (2008).

[37] F. I. Habbani and Khalda T. Osman, Appl. Radiat. Isot. **54**, 283 (2001).

[38] S. Chatterjee and A. Chatterjee, Nucl. Phys. A **125**, 593 (1969).

[39] Wen-deh Lu and R. W. Fink, Phys. Rev. C **4**, 1173 (1971).

[40] A. Yu. Konobeyev, V. P. Lunev, and Yu. N. Shubin, Nucl. Instrum. Methods B **108**, 233 (1996).

[41] S. Parashari *et al.*, in *Proceedings of the 19th International Scientific Conference on Electric Power Engineering (EPE)* (IEEE, Piscataway, NJ, 2018).

[42] J. F. Ziegler, Nucl. Instrum. Methods B **219-220**, 1027 (2004).

[43] C. H. Poppe *et al.*, Phys. Rev. C **14**, 438 (1976).

[44] J. W. Meadows and D. L. Smith, Neutrons from Proton Bombardment of Natural Lithium, Argonne National Laboratory Report No. ANL-7938, 1972, https://inldigitallibrary.inl.gov/Reports/ANL-7938.pdf.

[45] R. Makwana *et al.*, Phys. Rev. C **96**, 024608 (2017).

[46] D. L. Smith, J. W. Meadows, P. A. Moldauer, and W. P. Poenitz, Nucl. Phys. A **388**, 37 (1982).

[47] T. Vidmar, G. Kanish, and G. Vidmar, Appl. Radiat. Isot. **69**, 908 (2011).

[48] B. S. Shivashankar *et al.*, Nucl. Sci. Eng. **179**, 423 (2015).

[49] N. Otsuka *et al.*, Radiat. Phys. Chem. **140**, 502 (2017).

[50] R. Capote *et al.*, Nucl. Data Sheets **110**, 3107 (2009).

[51] A. J. Koning and J. P. Declaroche, Nucl. Phys. A **713**, 231 (2003).

[52] W. Hauser and H. Feshbach, Phys. Rev. **87**, 366 (1952).

[53] C. Kalbach, Phys. Rev. C **33**, 818 (1986).

[54] A. Gilbert and A. G. W. Cameron, Can. J. Phys. **43**, 1446 (1965).

[55] W. Dilg, W. Schantl, H. Vonach, and M. Uhl, Nucl. Phys. A **217**, 269 (1973).

[56] A. V. Ignatyuk, K. K. Istekov, and G. N. Smirenkin, Sov. J. Nucl. Phys. **29**, 450 (1979).

[57] A. V. Ignatyuk, J. L. Weil, S. Raman, and S. Kahane, Phys. Rev. C **47**, 1504 (1993).

[58] S. Goriely, S. Hilaire, and A. J. Koning, Phys. Rev. C **78**, 064307 (2008).

[59] S. Hilaire, M. Girod, S. Goriely, and A. J. Koning, Phys. Rev. C **86**, 064317 (2012).